AALBORG UNIVERSITY

DENMARK

Emulating UAV Air-to-Ground Radio Channel In Multi-Probe Anechoic Chamber

Miao, Yang; Fan, Wei; Rodrıguez-Pineiro, Jose; Yin, Xuefeng; Gong, Yi

Emulating UAV Air-to-Ground Radio Channel In Multi-Probe Anechoic Chamber

Yang MIAO

Dept. of Electrical and Electronic Engineering,
Southern University of Science and Technology,
Shenzhen, China
miaoy@sustc.edu.cn

Wei Fan

Dept. of Electronic Systems, Antenna, Propagation and Millimetre-wave Systems,
Aalborg University,
Aalborg, Denmark
wfa@es.aau.dk

José Rodríguez-Piñeiro

Dept. of Electronics and Information Engineering,
Tongji University,
Shanghai, China
j.rpineiro@tongji.edu.cn

Xuefeng Yin

Dept. of Electronics and Information Engineering,
Tongji University,
Shanghai, China
yinxuefeng@tongji.edu.cn

Yi Gong

Dept. of Electrical and Electronic Engineering,
Southern University of Science and Technology,
Shenzhen, China
gongy@sustc.edu.cn

Abstract—This paper proposes to use ray tracer to simulate unmanned aerial vehicles (UAV) air-to-ground (A2G) radio channels in various propagation environments and then to emulate ("replay") the acquired channels in multi-probe anechoic chamber for the purpose of testing UAV network terminal devices. The emulation accuracy of A2G channel by polarized plane wave synthesis algorithm assuming far-field is addressed, and emulated channel properties in the ascending process of UAV are evaluated.

Index Terms—Unmanned aerial vehicle air-to-ground channel, ray tracing, multi-probe anechoic chamber, fading emulation

I. INTRODUCTION

Unmanned aerial vehicles (UAV) assisted communication systems have been more accessible for civil uses lately. Applications such as aerial surveillance, transportation, disaster rescue operation, and agricultural management, are under deployment. [1] UAV assisted communications can be categorized into air-to-ground (A2G) and air-to-air (A2A) connections. While A2A is the particular scenario for multi-UAV networks, A2G connections are more likely to be exposed to complex and variable physical environments, especially in urban scenarios. In many countries, low altitude UAV platforms up to 100 m to 150 m are permitted by regulations. For instance, up to 120 m is allowed in USA, and 150 m in Japan. There are also restrictions on time when and region where UAV can fly, since improper operations or malfunctions of connection can cause danger to existing facilities and human beings. In view of communication engineers, it is important to study the characteristics of UAV A2G channel in low altitude, in order to optimize the UAV performance and the system design.

UAV A2G radio channel measurements have been reported in several works [2]–[6], including passive measurements based on commercial base stations, e.g. in live LTE networks, and active measurements where the transmitter is better controlled. Typical loads on UAV during channel measurement are the processor to control flight dynamics, the inertial unit to measure dynamics such as pitch, yaw and roll angles, the GPS, the GPS-disciplined rubidium oscillator, the wireless equipment to collect channel data, and the antennas to radiate or receive signals [1]. This is challenging for a small UAV, especially when multi-antenna channels or wideband channels are the target to measure. The load capacity of the UAV limits the size and weight of the measurement equipment, as well as their computational power.

Alternatively, deterministic simulation tools for network planning, e.g. ray tracing or propagation graph [7], can be used to predict the UAV A2G channel [8]–[10]. Those tools can save the high cost of conducting field measurements and avoid the safety concern. [9] simulated the A2G channel in urban, suburban, rural and over sea scenarios at 28 GHz and 60 GHz by ray tracer. [8] simulated the suburban area at L and C bands. Height dependent channel properties analyzed in ray traced models tell similar stories as the real world measured channel properties [3], [4], [11]. When UAV flies above rooftops, vegetation, and terrain elevations, A2G channel appears more like the free space propagation channel; when UAV flies in lower altitude, it sees more scatterers from buildings and rooftops, and A2G channel experiences high temporal/spatial variations and is non-stationary.

From above, we know that the small sized UAV communicating to/from ground when flying in low altitude is one important scenario to study on, and the A2G radio channel in different physical environments can be simulated by ray tracers. One step further, if measured or simulated A2G radio channels of various scenarios can be replayed in lab environment in a repeatable and controlled way, performances of UAV network terminal devices can be assessed. The replay of

Fig. 1. Channel emulator based multiprobe anechoic chamber

Fig. 2. Application scenario involving the UAV radio channel simulation and the channel emulation in multi-probe anechoic chamber

radio channel in lab environment is called **channel emulation**, and the testing of devices in emulated channel in lab is called **over-the-air (OTA) testing**. The purpose of channel emulation is to replay the desired spatial and temporal characteristics of intended electromagnetic fields inside the test zone. The purpose of OTA testing in laboratory is mainly to replace field trials on evaluating the performance of device under test (DUT). OTA testing of UAV in A2G channels is extremely appealing due to the fact that field trials in these propagation scenarios are very difficult and hard to control.

Fading emulator based multi-probe anechoic chamber (MPAC) [12]–[14], as is shown in Fig. 1, is one popular solution on OTA testing. In downlink, base station signals interacting with objects in target propagation environment are emulated, and the emulated signals are used to excite multiple probes; using the polarized radiation pattern of cross shaped probes, the probe locations and orientations, the desired electromagnetic fields can be generated on surface of test zone. The DUT in the center of test zone receives downlink signals from probes and then sends uplink signals to communication antenna, which is further connected to the base station emulator. The emulation accuracy depends on factors such as test zone size, probe number, measurement noise level, emulation algorithm, and non-ideality of setups.

The purpose of this paper is to simulate the UAV A2G radio channel in low altitude by ray tracer, and then to emulate the simulated channel in MPAC. As is shown in Fig. 2, this paper is instructive for testing UAV network terminal devices in anechoic chamber by emulating the UAV channel of real-world scenario. Since the A2G radio channel specially needs the modeling in three dimensions and highly variable elevation scatterers are expected at lower altitudes [15], the emulation accuracy with limited probe number and limited test zone size is stressed in this paper.

The structure for the rest of this paper is as follows. Section II describes the A2G radio channel simulation by ray tracer. Section III describes the channel emulation algorithm in MPAC. Section IV evaluates the emulation accuracy by analyzing the channel properties. Section V summarizes this paper.

Fig. 3. Propagation environment in ray tracing

II. Acquisition of UAV Air-to-Ground Radio Channel

The UAV A2G radio channel is simulated by the 3D ray tracer developed by Beijing Jiaotong University [16]. Propagation mechanisms like line-of-sight (LOS), specular reflection (up to the third order), and diffraction are included in the simulator, and nonspecular scattering is excluded. The input information is the thorough geometrical and electromagnetic description of the propagation environment, as well as the radiation properties of antennas. The propagation environment is a suburban campus of Technical University of Madrid, Spain. Included are buildings, factories, trees and metal containers. The simplified physical environment is shown in Fig. 3, which is the same as in [8]. Vertical transmit (Tx) and receive (Rx) antennas with isotropic radiation patterns are deployed in the center of the considered environment with elevation separation of 118.2 m, where Tx is assumed to be on a UAV and Rx on ground. Ascending process of UAV from ground to 100 m in constant speed is simulated at 1.2 GHz in this paper.

III. Channel Emulation in MPAC

The goal of channel emulation is to generate the desired electromagnetic fields in the test zone so that DUT can be tested in emulated channel in anechoic chamber as if it was tested in real-world measured or ray tracing simulated channel.
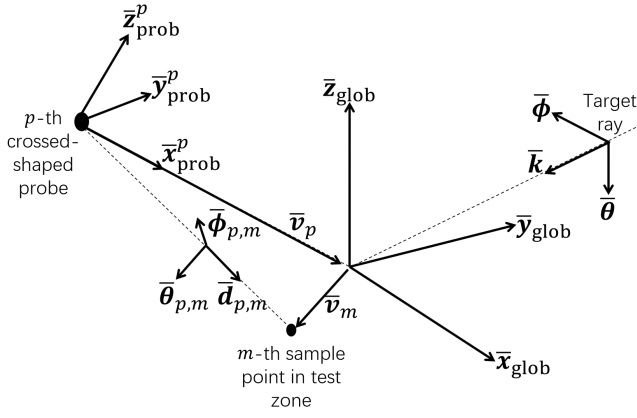
Fig. 4. Coordinate system in MPAC

Emulation algorithms are categorized into the prefaded signal synthesis (PFS) [12], [14] and the plane wave synthesis (PWS) [13], [17]. While PFS algorithm can reproduce stationary channels with a specific shape of power angular spectrum, PWS algorithm can reproduce dynamic multipath environment with time-varying PAS and also orthogonal polarizations of multipath. In PWS algorithm, a static plane wave with an arbitrary impinging angle can be generated within test area by allocating appropriate complex weights to the probes on the OTA ring. Either the simple mathematical approximation of plane wave [13] or the spherical wave theory [17] can be applied. In this paper, we utilize the former.

Referring to [13], the 3D polarized field synthesis by using plane waves is stated as follows. The coordinate system is shown in Fig. 4. Cartesian coordinate $[x, y, z]$ is convertible to spherical coordinate $[r, \theta, \phi]$, where θ in this paper indicates the co-elevation angle where $\theta = 0$ is the north pole and $\theta = \pi$ is the south pole of sphere. The probe radiation pattern is assumed constant in test zone; given that the test zone size is much smaller than the ring size, the variation of the radiation patterns of probes over small angles is ignored.

1) Target Ray: A target ray is characterized by the angle of arrival (AoA) $[\theta_R, \phi_R]$, complex gain α, and delay τ. An ideal plane wave is characterized by uniform amplitude distribution over the test zone and linear phase front along the propagation direction $\bar{k}$. The 3D polarized target field at m-th sample point is given by

$$\begin{bmatrix} e_m^x \\ e_m^y \\ e_m^z \end{bmatrix} = e_m \mathbf{A} \begin{bmatrix} 0 \\ \omega_\theta \\ \omega_\phi \end{bmatrix}. \tag{1}$$

e_m is the desired field at m-th sample point without information of polarization

$$e_m = \alpha \exp\left(-j\bar{k} \cdot \bar{v}_m\right) \tag{2}$$

where $\|\bar{k}\| = 2\pi/\lambda$, the unit vector of $\bar{k}$ is $[\sin(\theta_R)\cos(\phi_R), \sin(\theta_R)\sin(\phi_R), \cos(\theta_R)]$. Uniformly

distributed points on the spherical surface of test zone are used for sampling points, and

$$\mathbf{A} = \begin{bmatrix} \sin(\theta_R)\cos(\phi_R) & \cos(\theta_R)\cos(\phi_R) & -\sin(\phi_R) \\ \sin(\theta_R)\sin(\phi_R) & \cos(\theta_R)\sin(\phi_R) & \cos(\phi_R) \\ \cos(\theta_R) & -\sin(\theta_R) & 0 \end{bmatrix}. \tag{3}$$

The basic property of plane waves in free-space is that the directions of the electric and magnetic field vectors are orthogonal to the direction of propagation. Thus there are only two independent components of the target field whose two unit vectors are $\bar{\theta}$ and $\bar{\phi}$. $\bar{\theta}$, $\bar{\phi}$ and $\bar{k}$ form an orthonormal triad. The polarization information of the target field is given by ω_θ and ω_ϕ. For instance, $[\omega_\theta, \omega_\phi] = \left[\frac{1}{\sqrt{2}}, \frac{j}{\sqrt{2}}\right]$ is for right-handed circular polarization, and $[\omega_\theta, \omega_\phi] = \left[\frac{1}{\sqrt{2}}, \frac{1}{\sqrt{2}}\right]$ is for the linear polarization with positive slope.

2) Synthesized Ray: The synthesized polarized field at m-th sample point is given by

$$\begin{bmatrix} \tilde{e}_m^x \\ \tilde{e}_m^y \\ \tilde{e}_m^z \end{bmatrix} = \sum_{p=1}^{P} \mathbf{B}_p \cdot \beta_{p,m} \cdot \mathbf{A}_{p,m} \begin{bmatrix} 0 \\ g_p^\theta \\ g_p^\phi \end{bmatrix} \tag{4}$$

where $\beta_{p,m}$ is the propagation coefficient from p-th probe to m-th sample point, given by

$$\beta_{p,m} = \frac{\lambda}{4\pi\|\bar{v}_p + \bar{v}_m\|} \exp\left(-j\|\bar{k}\| \cdot \|\bar{v}_p + \bar{v}_m\|\right). \tag{5}$$

$\mathbf{A}_{p,m}$ is the transformation matrix converting the vector $\bar{d}_{p,m}$, $\bar{\theta}_{p,m}$ and $\bar{\phi}_{p,m}$ in local spherical coordinate to the vector $\bar{x}_{\text{prob}}^p$, $\bar{y}_{\text{prob}}^p$ and $\bar{z}_{\text{prob}}^p$ in local Cartesian coordinate. $\mathbf{A}_{p,m}$ has the same form as in (3) where θ_R, ϕ_R are replaced by $\theta_{k,m}, \phi_{k,m}$, respectively. g_p^θ and g_p^ϕ are the excitation voltages assigned for p-th cross-shaped probe.

$$\mathbf{B}_p = \begin{bmatrix} \cos(\gamma_{z3})\cos(\gamma_{z1}) - \sin(\gamma_{z3})\sin(\gamma_{x2})\sin(\gamma_{z1}), \\ -\cos(\gamma_{z3})\sin(\gamma_{z1}) - \sin(\gamma_{z3})\cos(\gamma_{x2})\cos(\gamma_{z1}), \\ \sin(\gamma_{z3})\sin(\gamma_{x2}); \\ \sin(\gamma_{z3})\cos(\gamma_{z1}) + \cos(\gamma_{z3})\cos(\gamma_{x2})\sin(\gamma_{z1}), \\ -\sin(\gamma_{z3})\sin(\gamma_{z1}) + \cos(\gamma_{z3})\cos(\gamma_{x2})\cos(\gamma_{z1}), \\ -\cos(\gamma_{z3})\sin(\gamma_{x2}); \\ \sin(\gamma_{x2})\sin(\gamma_{z1}), \\ \sin(\gamma_{x2})\cos(\gamma_{z1}), \\ \cos(\gamma_{x2}) \end{bmatrix} \tag{6}$$

is the right-handed transformation matrix from local probe coordinator characterized by $\bar{x}_{\text{prob}}^p$, $\bar{y}_{\text{prob}}^p$ and $\bar{z}_{\text{prob}}^p$ to global test zone coordinate characterized by $\bar{x}_{\text{glob}}$, $\bar{y}_{\text{glob}}$ and $\bar{z}_{\text{glob}}$. This transformation includes the coordinate rotation which is featured by Euler angle $[\gamma_{z1}, \gamma_{x2}, \gamma_{z3}]$. From the coordinate featured by $\bar{x}_{\text{prob}}^p$, $\bar{y}_{\text{prob}}^p$ and $\bar{z}_{\text{prob}}^p$, rotate about z_{prob}^p axis with angle γ_{z1} then we get coordinate $\left(x'^p_{\text{prob}}, y'^p_{\text{prob}}, z'^p_{\text{prob}}\right)$; rotate about x'^p_{prob} axis with angle γ_{x2} then we get coordinate $\left(x''^p_{\text{prob}}, y''^p_{\text{prob}}, z''^p_{\text{prob}}\right)$; rotate about z''^p_{prob} axis with angle γ_{z3} then we get the test zone coordinate featured by $\bar{x}_{\text{glob}}$, $\bar{y}_{\text{glob}}$ and $\bar{z}_{\text{glob}}$.

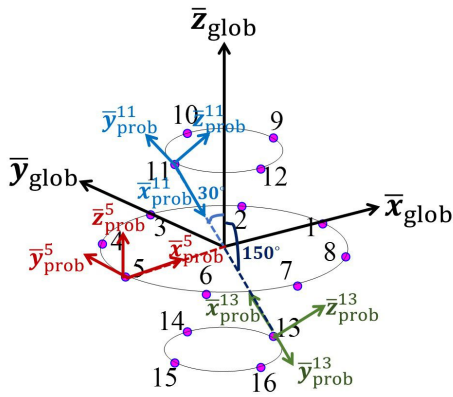In a typical F32 Propsium MPAC, totally 16 probes are deployed. As is shown in Fig. 5, in our chamber, probes 9-12

Fig. 5. Location of all probes in MPAC, and demonstration of the rotation from local probe coordinate to test zone coordinate

Fig. 6. Emulation error as to test zone radius

TABLE I
EULER ANGLES ROTATING LOCAL PROBE COORDINATE TO TEST ZONE COORDINATE

Probe index	γ_{z1}	γ_{x2}	γ_{z3}
1	π	0	0
2	$\frac{3}{4}\pi$	0	0
3	$\frac{1}{2}\pi$	0	0
4	$\frac{1}{4}\pi$	0	0
5	0	0	0
6	$-\frac{1}{4}\pi$	0	0
7	$-\frac{1}{2}\pi$	0	0
8	$-\frac{3}{4}\pi$	0	0
9	$\frac{1}{2}\pi$	$-\frac{1}{3}\pi$	$\frac{1}{2}\pi$
10	$\frac{1}{2}\pi$	$-\frac{1}{3}\pi$	0
11	$\frac{1}{2}\pi$	$-\frac{1}{3}\pi$	$-\frac{1}{2}\pi$
12	$\frac{1}{2}\pi$	$-\frac{1}{3}\pi$	π
13	$\frac{1}{2}\pi$	$\frac{1}{3}\pi$	$\frac{1}{2}\pi$
14	$\frac{1}{2}\pi$	$\frac{1}{3}\pi$	0
15	$\frac{1}{2}\pi$	$\frac{1}{3}\pi$	$-\frac{1}{2}\pi$
16	$\frac{1}{2}\pi$	$\frac{1}{3}\pi$	π

locate at elevation angle of $30°$ in global coordinate, probes 13-16 at $150°$, and the rest at $90°$ (in azimuth plane). The radius of the probe ring is 2 m. The Euler angles rotating the local probe coordinate to the test zone coordinate are shown in Table I.

From (1) and (4), g_p^θ and g_p^ϕ for $p = 1, 2, \ldots, P$ can be solved by least square solutions.

IV. NUMERICAL EXAMPLES

The relative error of emulated fields at sample points on surface of test zone is denoted by δ and is defined as

$$\delta = 10 \log_{10} \frac{\sum_m |\tilde{e}_m^x - e_m^x|^2 + |\tilde{e}_m^y - e_m^y|^2 + |\tilde{e}_m^z - e_m^z|^2}{\sum_m |e_m^x|^2 + |e_m^y|^2 + |e_m^z|^2}$$
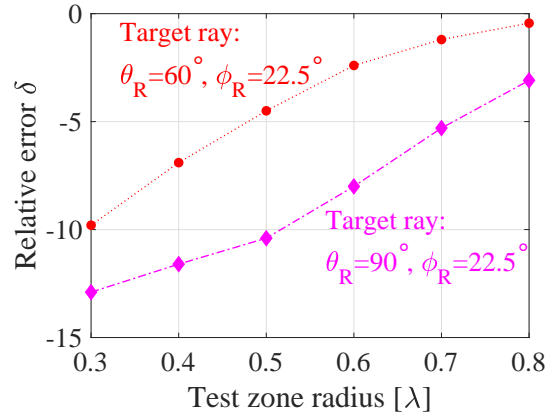
(7)

According to [18], the ratio between the radius of the test zone and the radius of the probe ring has to be under certain value to guarantee the field strength and phase stability across the test zone. The threshold can be set depending on the tolerance of correlation error, power imbalance, etc. Fig. 6 provides the plotting of the relative errors corresponding to different test zone radius. The relative error for each value of the radius tends to be converged with the increase of the density of sampling points. The plotting is for the single ray for the purpose of testing algorithm. The single ray with right-handed circular polarization is set as coming from $\{\theta_R = 90°, \phi_R = 22.5°\}$ (in azimuth plane, denoted as A), or from $\{\theta_R = 60°, \phi_R = 22.5°\}$ (in elevation plane, denoted as B). From the results, it can be seen that the emulation error increases with the increase of the test zone radius. Besides, the emulation error of ray A is smaller than that of ray B. It is within expectation since the angular separation of probes in azimuth domain is $45°$, which is smaller than $60°$ in elevation domain.

In the following content, the emulation of A2G channel by multi-probe and PWS algorithm is evaluated by comparing to the reference channel simulated by ray tracer, given the test zone radius of 0.5λ. The radio channel is the summation of rays.

Figure 7 (a)-(d) provide examples of emulated fields at the height of 10 m. In the four figures, discrepancies can be observed: while the maximum error among emulated rays is -6 dB, the minimum is -21.6 dB. The error of emulated channel comparing to the reference is -8 dB. Fig. 7 (e) presents the relative error δ of rays at all heights. Note that different number of rays are obtained for different height: when Tx is at lower altitude, multipath with many reflections and diffraction are observed; with the increase of height, multipath components decrease and direct path remains. It is obvious from figure that different rays are emulated with different accuracy, depending on the directional properties of the impinging wave. The essential theory behind the MPAC is to approximate the desired tangential fields on surface of test zone by several probes. For a target ray whose impinging di-

rection is between probes, the emulation error would probably be larger than the ray coming from the direction of a probe. That explains why at lower height with rich multipath, the emulation error varies a lot. Fig. 7 (f) presents the averaged relative error on all rays at each height and the confidence level. It can be seen that the average error at lower UAV altitude is smaller than that at higher UAV altitude. It owes to the configuration of probes and the AoA of rays. From Fig. 8, with the increase of UAV altitude, rays tend to come from more diverse elevation angles (co-elevation angle θ_R). But as is shown in Fig. 5, probes 9-12, 13-16 that are lying in co-elevation angles of $30°$ and $150°$ respectively, and are used to capture rays coming from above horizon or below horizon (θ_R other than $90°$), are more sparsely deployed than the probes 1-8 that are used to capture rays coming from horizon plane (θ_R of $90°$).
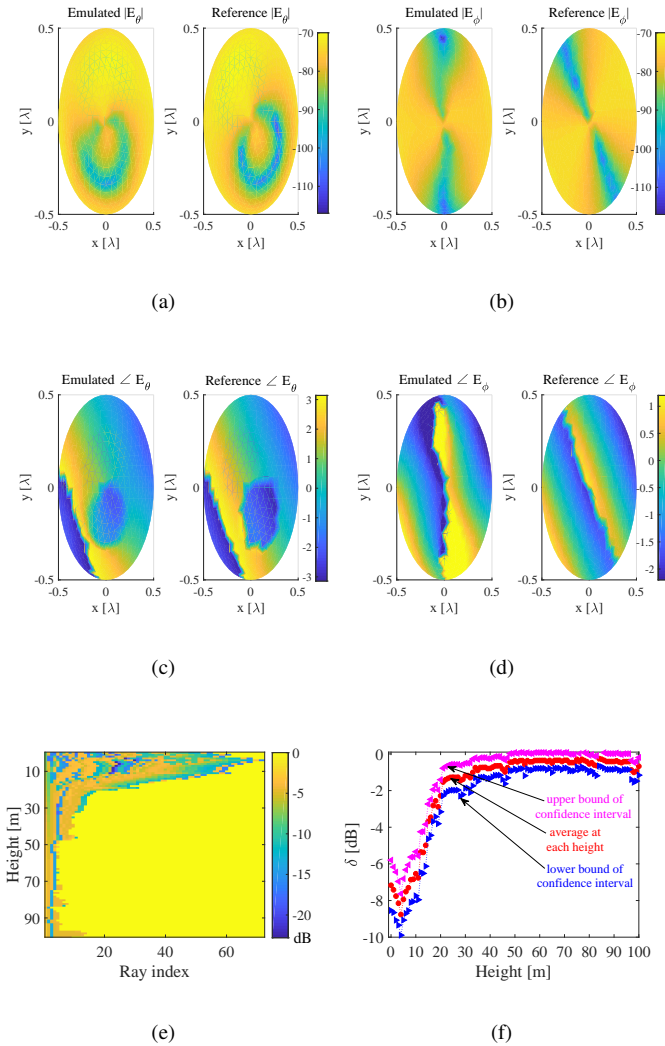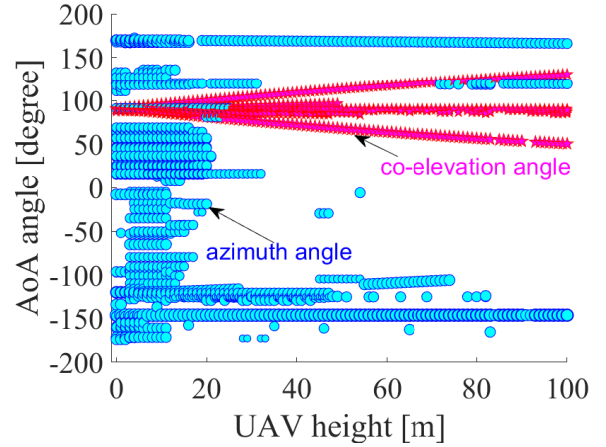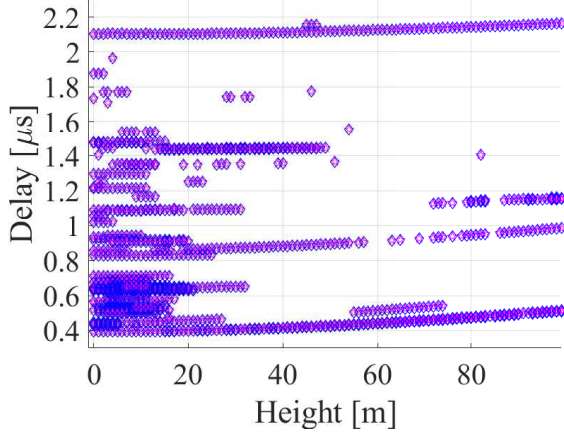

Fig. 8. AoA of all rays at all heights, where the marker size indicates the power

In addition, the power delay height profile is shown in Fig. 9. From Fig. 9 (a), it can be seen that the emulated channel resembles the reference for the delays at all heights. From Fig. 9 (b), the emulated PDP has integral power discrepancy comparing to the reference PDP; however, if with power compensation or normalization, the emulated PDP resembles to the reference. This is within expectation, because the power delay profile is not a limiting factor for the channel emulator. With one single probe, we can already emulate arbitrary power angular delay profile. In addition, in Fig. 9 (b), the power level is too low to be detected in real channel emulation measurement, hence normalization of power is necessary.
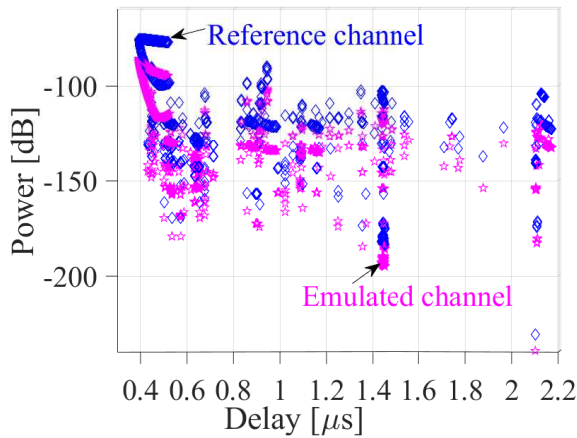
Fig. 10 (a) shows the mean delay τ_m and the rms delay spread σ_τ of emulated and reference channels, and Fig. 10 (b) shows the absolute differences of τ_m, σ_τ between the emulated and the reference. τ_m and σ_τ are defined the same as in [8]. From observations on figures, the mean delay of emulated channel tends to have slight discrepancy at higher UAV altitude; the rms delay spread of emulated channel resembles to the reference perfectly, telling the same story that the delay spread increases with the increase of UAV altitude until reach its maximum at around 50-70 meters, then decrease due to the dominance of direct path.

V. CONCLUSION

This paper demonstrated an application scenario combining ray tracing simulation and channel emulation in multi-probe anechoic chamber for UAV A2G connections. On one hand, utilizing ray tracer for network planning and radio channel simulation is a cost-effective solution, especially when field measurement is difficult or too expensive to implement. Ray tracing simulated radio channel presents the similar properties as the measured ones, and it can be used to obtain radio channel in various propagation scenarios. On the other hand, the obtained channel in various scenarios can be replayed in anechoic chamber and then be used for testing UAV network devices. This paper addressed the emulation accuracy in the numerical examples. It is found that the emulation accuracy
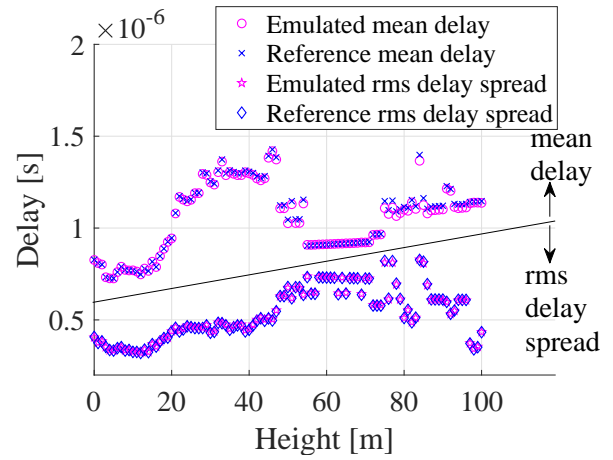

Fig. 7. Example of emulated and reference fields on surface of test zone when UAV is at height 10 m: (a) amplitude of E_θ (b) amplitude of E_ϕ (c) phase of E_θ (d) phase of E_ϕ; (e) emulation error at each height for each ray; (f) average emulation error, and its upper/lower bounds of confidence interval with 95% confidence at each height

(a)

(b)

Fig. 9. The power delay height profile, where the legends of markers in (a) and (b) are the same

(a)

(b)

Fig. 10. (a) The values (b) the absolute errors of respectively the mean delay and the rms delay spread of emulated and reference channel at different UAV height
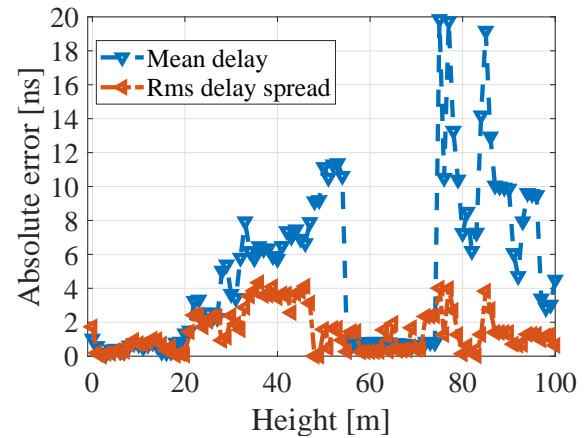
varies for rays coming from diverse elevation angles, due to the restriction of probe configuration in the standard F32 Propsium emulation system. Nevertheless, the channel properties like power delay profile and delay spread, can be accurately emulated. In the future studies, UAV A2G radio channel in various propagation scenarios will be modeled, emulation of channels characterized by measurements will be evaluated, and UAV terminal devices will be tested.

REFERENCES

[1] A.A. Khuwaja, Y. Chen, N. Zhao, M.S. Alouini, "A survey of channel modeling for UAV communications," submitted.

[2] M. Simunek, F.P. Fontan, and P. Pechac, "The UAV low elevation propagation channel in urban areas: statistical analysis and time-series generator," *IEEE Trans. Antennas Propag.*, vol. 61, no. 7, pp. 3850-3858, 2013.

[3] X. Cai, A.G. Plaza, D. Alonso, L. Zhang, C.B. Rodriguez, A.P. Yuste, and X. Yin, "Low altitude UAV propagation channel modeling," in *Proc. 11th Eur. Conf. Antennas Propag.*, Paris, France, pp. 1443-1447, Mar. 2017.

[4] R.M. Gutierrez, H. Yu, Y. Rong, and D.W. Bliss, "Time and frequency dispersion characteristics of the UAS wireless channel in residential and mountainous desert terrains," in *Proc. IEEE Annual Consumer Commun. Netw. Conf.*, Las Vegas, UAS, pp. 516-521, Jan. 2017.

[5] X. Ye, X. Cai, X. Yin, J. Rodriguez-Pineiro, L. Tian, J. Dou,"Air-to-ground big-data-assisted channel modeling based on passive sounding in LTE Networks", in *IEEE Globecom Workshops 2017*, Dec. 2017.

[6] Z. Qiu, X. Chu, C. Calvo-Ramirez, C. Briso, X. Yin, "Low altitude UAV air-to-ground channel measurement and modeling in semiurban environment," *Wireless Communications and Mobile Computing*, vol. 2017, no. 1587412, Nov. 2017.

[7] R. Adeogun, T. Pedersen, "Propagation graph based model for polarized multiantenna wireless channels," in *Proc. IEEE Wireless Commun. Netw. Conf.*, Barcelona, Spain, Jan. 2018.

[8] X. Chu, C. Briso, D. He, X. Yin, and J. Dou, "Channel modeling for low-altitude UAV in suburban environments based on ray tracer," in

Proc. 12th Eur. Conf. Antennas Propag., London, UK, Apr. 2018.

[9] W. Khawaja, O. Ozdemir, and I. Guvenc, "UAV air-to-ground channel characterization for mmWave systems," in *Proc. IEEE 86th Vehicular Technology Conf.*, Toronto, Canada, Sep. 2017.

[10] K. Daniel, M. Putzke, B. Dusza, and C. Wietfeld, "Three dimensional channel characterization for low altitude aerial vehicles," in *Proc. 7th Int. Symp. Wireless Commun. Syst*, York, UK, Sep. 2010.

[11] R. Amorim, H. Nguyen, P. Mogensen, I.Z. Kovacs, J. Wigard, and T.B. Sorensen, "Radio channel modeling for UAV communication over cellular networks," *IEEE Wireless Commun. Lett.*, vol. 6, no. 4, Aug. 2017.

[12] P. Kyosti, T. Jamsa, J.P. Nuutinen, "Channel modeling for multiprobe over-the-air MIMO Testing," *Int. J. Antennas Propag.,* vol. 2012, no. 615954, Mar. 2012.

[13] F. Wei, I. Carton, P. Kyosti, and G.F. Pedersen, "Emulating ray-tracing channels in multiprobe anechoic chamber setups for virtual drive testing," *IEEE Trans. Antennas Propag.*, vol. 64, no. 2, Feb. 2016.

[14] W. Fan, X. Carreo, J. Nielsen, J.S. Ashta, G.F. Pedersen, M.B. Knudsen, "Verification of emulated channels in multi-probe based MIMO OTA testing setup," in *Proc. 7th Eur. Conf. Antenna Propag.,* Gothenburg, Sweden, Apr. 2013, pp. 97-101.

[15] L. Zeng, X. Cheng, C.X. Wang, and X. Yin, "A 3D geometry-based stochastic channel model for UAV-MIMO channels," in *Proc. IEEE Wireless Commun. Netw. Conf.*, San Francisco, USA, Mar. 2017.

[16] K. Guan, Z. Zhong, B. Ai, and T. Kurner, "Deterministic propagation modeling for the realistic high-speed railway environment," in *Vehicular Technology Conference,* Dresden, Germany, Jun. 2013.

[17] A. Khatun, V.M. Kolmonen, V. Hovinen, D. Parveg, M. Berg, K. Haneda, K.I. Nikoskinen, E.T. Salonen, "Experimental verification of a plane-wave field synthesis technique for MIMO OTA antenna testing," *IEEE Trans. Antennas Propag.*, vol. 64, no. 7, Jul. 2016.

[18] P. Kyosti, L. Hentila, "Criteria for physical dimensions of MIMO OTA multi-probe test setup," in *Proc. 6th Eur. Conf. Antenna Propag.,* Prague, Czech Republic, pp. 2164-3342, Jun. 2012.